OPEN ACCESS



Possible Evidence for Shear-driven Kelvin-Helmholtz Instability along the Boundary of Fast and Slow Solar Wind in the Corona

Daniele Telloni¹, Laxman Adhikari², Gary P. Zank^{2,3}, Lingling Zhao², Luca Sorriso-Valvo^{4,5}, Ester Antonucci¹, Silvio Giordano¹, and Salvatore Mancuso¹

National Institute for Astrophysics, Astrophysical Observatory of Torino, Via Osservatorio 20, I-10025 Pino Torinese, Italy; daniele.telloni@inaf.it
Center for Space Plasma and Aeronomic Research, University of Alabama in Huntsville, Huntsville, AL 35805, USA
Department of Space Science, University of Alabama in Huntsville, Huntsville, AL 35805, USA
Swedish Institute of Space Physics, Ångström Laboratory, Lägerhyddsvägen 1, SE-751 21 Uppsala, Sweden
National Research Council, Institute for the Science and Technology of Plasmas, Via Amendola 122/D, I-70126 Bari, Italy
Received 2021 November 1; revised 2022 February 16; accepted 2022 March 1; published 2022 April 15

Abstract

This paper reports the first possible evidence for the development of the Kelvin–Helmholtz (KH) instability at the border of coronal holes separating the associated fast wind from the slower wind originating from adjacent streamer regions. Based on a statistical data set of spectroscopic measurements of the UV corona acquired with the UltraViolet Coronagraph Spectrometer on board the SOlar and Heliospheric Observatory during the minimum activity of solar cycle 22, high temperature–velocity correlations are found along the fast/slow solar wind interface region and interpreted as manifestations of KH vortices formed by the roll-up of the shear flow, whose dissipation could lead to higher heating and, because of that, higher velocities. These observational results are supported by solving coupled solar wind and turbulence transport equations including a KH-driven source of turbulence along the tangential velocity discontinuity between faster and slower coronal flows: numerical analysis indicates that the correlation between the solar wind speed and temperature is large in the presence of the shear source of turbulence. These findings suggest that the KH instability may play an important role both in the plasma dynamics and in the energy deposition at the boundaries of coronal holes and equatorial streamers.

Unified Astronomy Thesaurus concepts: Magnetohydrodynamics (1964); Theoretical models (2107); Time series analysis (1916); Solar corona (1483); Solar coronal heating (1989); Solar coronal holes (1484); Solar coronal streamers (1486); Solar oscillations (1515); Solar ultraviolet emission (1533)

1. Introduction

For extended periods during 1996, at the solar cycle 22 activity minimum, the outer solar corona was simply formed by an equatorial streamer belt separating the large coronal holes present at the poles (Schwenn et al. 1997). This configuration was predominantly shaped by the magnetic dipole, whose axis was nearly perpendicular to the heliographic equator at that time. This basic magnetic topology of the solar atmosphere and its heliospheric extension was observed with an unprecedented set of space instruments, thanks to the launch of Ulysses in 1990 (Wenzel et al. 1992) and the SOlar and Heliospheric Observatory (SOHO) in 1995 (Domingo et al. 1995). For the first time, the corona was observed both in visible light, over a broad field of view extending continuously from 1.1 to 30 R_{\odot} , with the three coronagraph package of the Large Angle Spectrometric COronagraph (LASCO) instrument suite (Brueckner et al. 1995) on board SOHO, and in the emission of resonantly scattered ultraviolet lines, which depends on the expansion rate of the coronal plasma, with the SOHO/ UltraViolet Coronagraph Spectrometer (UVCS; Kohl et al. 1995). Hence, the speed of the solar wind could be directly measured in the corona during the initial phase of its propagation into the heliosphere. At the same time, the heliosphere was explored by Ulysses in its out-of-ecliptic journey: the spacecraft in situ instruments crossed the

Original content from this work may be used under the terms of the Creative Commons Attribution 4.0 licence. Any further distribution of this work must maintain attribution to the author(s) and the title of the work, journal citation and DOI.

latitudinal zones where the fast and slow wind were predominant, with the slow wind confined in an equatorial belt $\pm 20^{\circ}$ wide (McComas et al. 1998).

The crucial role of the magnetic field and its divergence in regulating the characteristics of the solar wind was proposed by many authors on the basis of early space observations and modeling of the solar atmosphere (Kopp & Holzer 1976; Levine et al. 1977; Withbroe 1988; Wang & Sheeley 1990). The capability of measuring the wind in the solar atmosphere, introduced with UVCS during the 1996 solar minimum, confirmed model predictions that the magnetic field channels the fast wind in the core of coronal holes, where the superradial field lines are less divergent, and the slow wind in their peripheral layers, where the lines diverge rapidly toward the streamer boundary and extend farther out, in regions adjacent to the current sheet that forms beyond the streamer cusp between opposite magnetic polarities.

In the core of coronal holes, where the areal expansion of the magnetic field is the least, the ${\rm O}^{+5}$ ions of the solar wind can be traced from 1.5 R_{\odot} (Kohl et al. 1998; Cranmer et al. 1999; Antonucci et al. 2000) to 5 R_{\odot} (Telloni et al. 2007a). In this interval they are accelerated from 40 km s⁻¹ to speeds in the range of 550–760 km s⁻¹, approaching the asymptotic wind speed corresponding to heliospheric high-speed streams. The observed wind speed then decreases from the core to the borders of coronal holes, thus establishing empirically the anticorrelation of the outflow velocity with the areal divergence of the magnetic field. As the field expansion factor increases toward the edges of the coronal holes (e.g., Dobrzycka et al. 1999, who estimated a divergence factor ranging from 6 to 7.5),

the wind at 3.5 R_{\odot} slows down from polar values of about $400 \,\mathrm{km \ s^{-1}}$ (e.g., Telloni et al. 2007a) to about 110 km s⁻¹ (Antonucci et al. 2005; Abbo et al. 2010). The slowest wind, however, is observed to correspond to nonmonotonic expansion of field lines, that is, diverging and then converging lines such as those separating substreamers in the complex equatorial streamers present at solar minimum (Noci & Gavryuseva 2007) and at the interface between streamers and coronal holes (Wang 1994; Antonucci 2006; Antonucci et al. 2012). During the minimum activity year 2020, the Metis coronagraph (Antonucci et al. 2020b) on board Solar Orbiter (Müller et al. 2020) has recently explored the hydrogen component of the solar wind within $\pm 10^{\circ}$ from the equatorial current sheet. This has been found to flow at about $95-185 \text{ km s}^{-1}$ between 3.5 and 6.3 R_{\odot} (Romoli et al. 2021; Telloni et al. 2021). In summary, the open magnetic field lines, filling the entire outer corona beyond a few solar radii, originate primarily from polar holes with an expansion factor varying with heliolatitude: the field divergence, lowest in the core, the source of the fast wind, rapidly increases toward the borders of the polar holes and peaks close to the hole-streamer interface, the source of the slow wind. The coronal wind results obtained with UVCS have been recently reviewed by Abbo et al. (2016), Cranmer et al. (2017), and Antonucci et al. (2020a).

Not only is the coronal expansion rate anticorrelated with the field divergence, as are other physical parameters, such as the width of the velocity distribution of the oxygen ions (measuring the ion kinetic temperature), which decreases from the polar regions to the borders of the coronal holes. In the core of polar holes, the observed OVI line width, determined by the ion velocity distribution across the magnetic field, largely exceeds the value expected for thermal equilibrium, as well as that along the magnetic field. The degree of anisotropy of the ion velocity distribution reaches its maximum value at about 2.9 R_{\odot} (Telloni et al. 2007b). These observations indicate that energy is preferentially deposited (presumably via ion cyclotron resonance scattering of high-frequency Alfvén waves; Kohl et al. 1998; Cranmer et al. 1999) in the coronal plasma beyond the sonic point, which is located at 1.9 R_{\odot} according to a statistical study by Telloni et al. (2019b), with the effect of rapidly increasing the wind speed to the fast wind regime. The ion kinetic temperature decreases toward the coronal hole boundary by about one order of magnitude: from $\ge 10^8$ K in the core to about 10^7 K at the borders of coronal holes (see Antonucci et al. 2005). Therefore, this suggests that energy is released also in these regions, although to a lesser degree than at the poles. It is worth noting that an increase of oxygen kinetic temperature is also observed within streamers, although this effect is lower than in the open magnetic field regions (Frazin et al. 2003).

The boundaries between closed and open field lines along the streamer and the streamer top are predicted to be the site of local dynamical effects involving reconnection processes and release of plasma. These are observed, for instance, in the form of coronal blobs with propagation characteristics similar to those of the slow wind or of reconnection events close to the current sheet in the corona (Sheeley et al. 1997; Wang et al. 2000). More importantly, the boundary regions between the fast solar wind originating from coronal holes and the slow solar wind flowing from equatorial streamers may be unstable to the Kelvin–Helmholtz (KH) instability, as illustrated in Figure 1. In fact, the increase in velocity can be very rapid

across the lateral sides of the streamers, as clearly shown by Noci & Gavryuseva (2007).

The KH instability arises at the interface between two fluids in parallel motion with different shear velocities. This flowdriven instability drives the shear sheet to roll up into vortexlike structures. The KH instability can thus be regarded as a dynamic process whereby shear velocity is transferred to rotational vorticity. According to linear stability theory (see Faganello & Califano 2017, and references therein), the perturbations grow exponentially with a characteristic rate and are of a single dominant scale. However, since the boundary layers between the KH vortex-shaped features and the unperturbed solar corona may be themselves unstable to the KH instability and also to the Rayleigh-Taylor instability, secondary instabilities growing along the vortex arms can completely disrupt the vortex structure driving the formation of a turbulent, self-similar mixing layer. In this nonlinear phase, the plasma instabilities, initially well distinct during the early linear stage, comprise a superimposition of many modes, namely, a spectrum, that interact nonlinearly with each other in a turbulent cascade down to scales where the energy initially provided by the velocity shear is eventually dissipated to heat the fast/slow wind interaction region plasma. The dissipation of the KH turbulence driven on the boundaries of the coronal hole may thus participate in energy deposition in the solar corona, together with other possible physical mechanisms. The KH mechanism can heat the coronal plasma also in the initial linear stage, namely, even without the dissipation of a turbulent spectrum, provided that the KH vortices last long enough to reach a critical configuration unstable to magnetic reconnection. As the magnetic field lines are frozen in the fluid, they are folded and twisted by the KH vortical fluid motions in an antiparallel geometry. As a consequence, the kinetic energy associated with KH vortices is converted into magnetic energy. The wrapping of the magnetic field along the KH structures continues until the oppositely directed field lines reconnect, thereby dissipating the stored magnetic energy into thermal energy (Matsumoto & Hoshino 2004), which heats the coronal region adjacent to the coronal hole boundary.

It is well known that magnetic fields stabilize the KH instability from the perspective of theoretical and idealized linear calculations such as those presented in Chandrasekhar (1961), which imply that the velocity shear must be super-Alfvénic to lead to the generation of the KH instability. However, it is by no means clear that more complex and typical environments such as the solar corona resemble such idealized conditions. The argument for suppression of the KH instability assumes that the magnetic fields and the flow across a boundary are highly aligned. If the magnetic field is more azimuthal, the restoring tension is reduced and the flow can be more susceptible to KH instability. In the extreme situation of a magnetic field orthogonal to two tangential streams, the sheared flow is always unstable to the KH instability, just as in the hydrodynamic case, even for subsonic flows, and the magnetic field basically plays no role. If such nontangential magnetic field conditions occur in the low solar corona, as might be expected, various forms of interchange reconnection can occur along the boundaries of nominally fast and slow wind where loops and open field collide, leading to current sheet formation and magnetic fields that cross from one side of what was a tangential flow to the other. For instance, Schwadron & McComas (2021) argue that nontangential magnetic fields crossing shearing flows can be the origin of

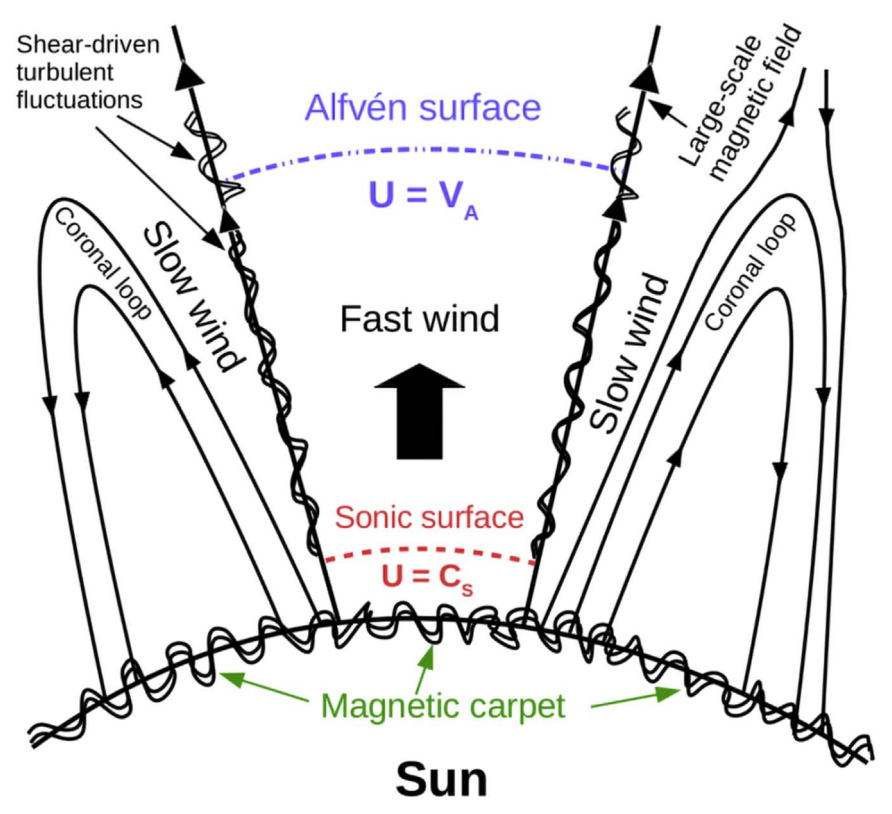


Figure 1. Cartoon illustrating the possible initiation of shear-driven turbulent fluctuations associated with the development of the KH instability along the boundaries of a coronal hole that separate faster and slower coronal flows. The sonic and Alfvén surfaces (where the coronal plasma speed equals those of sound C_s and Alfvén waves V_A , respectively) are also shown. Adapted from Figure 1 of Zank et al. (2021).

switchbacks. So the existence of switchbacks may, in their interpretation, be a manifestation of nontangential magnetic fields associated with tangential flows as well. In these regions, very complicated structures with a weak and probably quite disordered magnetic field can arise. The simple idealized KH instability of Chandrasekhar (1961) is certainly unlikely to occur, and the KH instability may resemble its gasdynamic form instead. Hence, despite previous studies that investigated the conditions for the onset of KH instability in the solar wind and in coronal plumes (e.g., Parhi et al. 1999; Velli et al. 2011) and concluded that the KH instability may arise only in super-Alfvénic regions, at distances larger than $10 R_{\odot}$ (Velli et al. 2011 found that the KH instability could become important at 0.2-0.3 au), the KH instability has been widely imaged in the sub-Alfvénic low solar corona, at distances well below 10 R_{\odot} , in strong magnetic field environments associated with active regions (Yuan et al. 2019), at the flanks of coronal mass ejections (Foullon et al. 2011; Ofman & Thompson 2011; Foullon et al. 2013; Möstl et al. 2013; Nykyri & Foullon 2013), along solar prominence/corona discontinuity layers (Berger et al. 2010; Ryutova et al. 2010; Hillier & Polito 2018; Yang et al. 2018), in solar jets (Kuridze et al. 2016; Li et al. 2018), associated with streamer wave phenomena (Feng et al. 2013), and in white-light eclipse observations (Druckmüller et al. 2014). This is because the realistic solar corona is quite unlike a nice cartoon showing well-defined large-scale magnetic field lines; rather, at least locally, it is characterized by a very complex magnetic topology. The onset of the KH instability depends on the orientation of the magnetic field relative to the tangential flows. It follows that even the sub-Alfvénic velocity shear along the fast/slow boundary in the solar corona can lead to KH instability growth, provided that, as expected, the streamer belt

region does not have a nicely ordered magnetic field and instead possesses locally a very complicated structure with a non-tangential magnetic field configuration. Although theoretically predicted to play an important role in the plasma dynamics between high- and low-speed coronal streams flowing alongside each other (Ismayilli et al. 2018), the KH instability has not yet been detected at the edges of coronal holes adjacent to equatorial streamers, where shear due to the outflow of fluids with different velocities can initiate KH vortices. This lack of evidence motivates the present work, which indeed aims at providing, for the first time, possible observational evidence for manifestations of the KH instability in the solar corona in the interaction region between fast and slow solar wind.

Simplifying the basic properties of the KH instability discussed above, the greater the velocity shear, the greater the formation of KH vortices and, therefore, the greater the energy deposited through the KH mechanism to the coronal plasma (say, the higher the kinetic temperature T). This eventually leads to higher solar wind velocities U. The large, coherent KH vortices along the hole/streamer interface and their global effects on the coronal plasma (i.e., the driven turbulent layer, which increases in size as the KH instability develops and where energy is nonlinearly transferred down to dissipative scales, thus heating the plasma) might be (albeit indirectly) revealed as well-correlated fluctuations of the velocity U and temperature T of the outflowing plasma. The only coronagraph capable of providing information on both the speed and temperature of the coronal plasma is UVCS, whose data in this paper are analyzed statistically in order to search for T-U temporal correlations, which are expected to be higher where the KH instability develops. As shown in Section 2, during solar minimum, the coronal regions with the highest T-U correlations lie at the flanks of the equatorial streamers, thus supporting the view of the KH instability arising along the fast/slow wind boundary in the corona. The presented findings are supported by a spectral theory for nearly incompressible magnetohydrodynamics (MHD) assuming a KH-induced shear driving turbulence (Section 3). Concluding remarks are given in Section 4.

2. UVCS Data Analysis

The UVCS instrument on board SOHO, operating almost continuously from 1996 to 2012, provided spectroscopic measurements of the extended solar corona from two UV spectrometric channels, optimized for observing the H I Ly α spectral line at 1215.67 Å and the O VI doublet at 1031.92 and 1037.61 Å. The UVCS instantaneous field of view is determined by the instrumental entrance slit, which images a region of 40′, in the direction perpendicular to the radial, and up to 84″ wide in the radial direction. The slit can be positioned at any distance from the Sun between 1.2 and 10 R_{\odot} and at any position angle to cover the entire corona (the reader is referred to Kohl et al. 1995 for a complete description of the UVCS instrument).

The present study focuses on the solar cycle 22 activity minimum and, specifically, from Carrington Rotation (CR) 1909 to CR 1925 (namely, from 1996 May 5 to 1997 August 12), when the magnetic dipole configuration shaping the solar corona was particularly stable, as well as, consequently, the coronal hole/streamer boundary (Strachan et al. 2012). In that period, UVCS performed a daily synoptic observation program to scan (albeit not uniformly) the entire 360° solar corona, at eight different position angles separated by an angular step of 45°, with the observed heliocentric distances ranging from \sim 1.5 to \sim 3.0 R_{\odot} at equatorial regions, \sim 2.25 R_{\odot} at midlatitudes, and \sim 2.5 R_{\odot} at polar latitudes (a more detailed description of UVCS synoptic observations is reported in Giordano & Mancuso 2008).

The synoptic program occupied a little more than half of the observation time, so in this study the so-called special observations, carried out every day by aiming at specific targets in the corona, are also used. This allows for increased statistics and temporal and spatial coverage.

The raw UVCS data employed in the present paper can be retrieved from the SOHO archive. 6 Proper calibration of UVCS data (also accounting for temporal variations in instrument performances; Gardner et al. 2002) has been performed with the last release of the UVCS Data Analysis Software (DAS; ver. 51), available at the UVCS website. The order to increase the statistics, in each observation all the subsequent exposures with the same instrumental setup (such as mirror pointing, slit width, spatial binning, and spectral binning) have been summed together, and the data have been furthermore rebinned to a number of spatial elements along the slit corresponding to an angular dimension of 5°. This last expedient, in particular, is the right compromise between the desired increase in statistics and a spatial coverage as uniform as possible. After selecting the spectral windows where the O VI doublet is detected, the estimated background for each observation is subtracted. The total intensity of both lines and the width of the most intense O VI $\lambda 1032$ spectral line are finally computed.

Since the statistics are not always sufficiently reliable to allow a fit of the spectral line with a Gaussian profile that accounts for the instrumental effects, following Telloni et al. (2019b), the width of the oxygen velocity distribution is defined through the second central moment, i.e., the variance, of the O VI $\lambda 1032$ spectral line as

$$\mu_2 = \frac{\sum_{i=0}^{N} (\lambda_i - \overline{\lambda})^2 P(\lambda_i)}{\sum_{i=0}^{N} P(\lambda_i)},\tag{1}$$

where $P(\lambda_i)$ is the measured spectrum after background subtraction at the wavelength λ_i in the *N*-point spectral window and $\overline{\lambda} \simeq 1032$ Å is the line centroid. It is worth pointing out that assuming the same instrumental configuration, as in this analysis, ensures that the instrumental effects result just in a constant offset to the line width for each UVCS measurement at each location in the solar corona. Therefore, this does not affect the estimate of the temporal correlation that this work aims to look for between the line width of the oxygen ions, i.e., their kinetic temperature, and the plasma velocity.

The UVCS-based spectroscopic measurements are used to gather information on crucial quantities in the solar corona. Specifically, as first adopted by Noci & Gavryuseva (2007) in the analysis of plasma outflows in coronal streamers and recently taken up by Telloni et al. (2019b) in the study of polar fast winds, the $\lambda 1037/\lambda 1032$ line intensity ratio ρ can be regarded as a proxy of the radial outflow speed U in both quiescent streamers and open-field regions. The reader is referred to the two aforementioned papers for a fairly complete discussion on this diagnostic approach. As for the width of the velocity distribution function of the emitting oxygen ions, the line broadening is due to both thermal and turbulent/wave motions. It follows that the variance μ_2 of the O VI $\lambda 1032$ spectral line comprises both of these contributions and is thus a measure of the kinetic temperature T of the oxygen ions and, ultimately, of the energy deposited to the oxygen component of the solar wind.

Through this comprehensive data reduction and by taking advantage of both the synoptic and the special observation program, the O VI $\lambda 1032$ line intensity and variance μ_2 and the O VI doublet intensity ratio ρ are obtained for the entire solar corona with an angular resolution of 5° and at (discrete) heliocentric distances ranging from 1.4 to 2.3 or 3.3 R_{\odot} depending on the latitude. Altogether, these relevant quantities have been inferred in 379 points of the solar corona throughout the analyzed period. An overview of these spectroscopic quantities can be represented by the corresponding Carrington maps, obtained by collecting all the data at a distance between 2.0 and 2.5 R_{\odot} for the entire period of interest and after some interpolation along each latitudinal profile in order to make a uniform grid (Figure 2).

As can be readily seen from both the oxygen UV radiance (Figure 2(a)) and the proxies for the oxygen kinetic temperature T (Figure 2(b)) and speed U (Figure 2(c)), the magnetic dipole geometry characterized by large, long-lived polar coronal holes separated from a near-equatorial streamer belt is very stable in the selected time period. The fainter northern and southern polar coronal holes, $\sim 90^\circ$ wide at 2.0–2.5 R_\odot , are the sources of a hotter, faster outflowing plasma, as evidenced by the higher values of the O VI $\lambda 1032$ variance μ_2 and O VI doublet intensity ratio ρ (Figures 2(b) and (c), respectively). Conversely, a cooler, slower solar wind originates from the brighter

⁶ https://sohowww.nascom.nasa.gov/data/archive/

https://lweb.cfa.harvard.edu/uvcs/

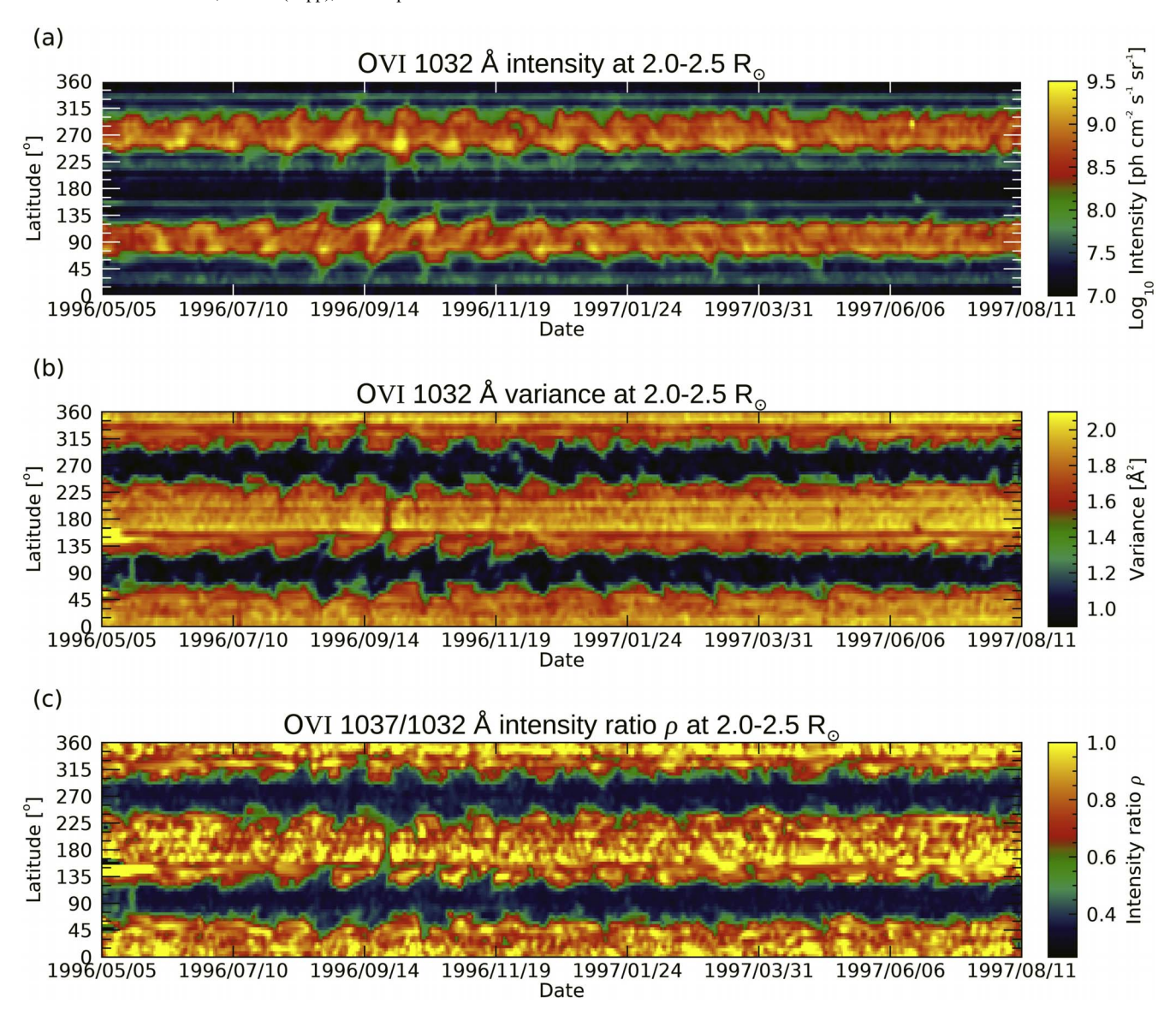


Figure 2. Carrington maps of (a) the O VI λ 1032 intensity and (b) variance μ_2 and of (c) the O VI λ 1037/ λ 1032 intensity ratio ρ , at 2.0–2.5 R_{\odot} , in the time period from 1996 May 5 to 1997 August 12. Latitudes, i.e., position angles, are counterclockwise from the north pole.

equatorial streamer belt $\sim 60^\circ$ wide at $2.0-2.5~R_\odot$. Noteworthy is that the stability of the magnetic configuration of the solar corona ensures that the location of the coronal hole/streamer boundaries, where the dynamical effects of velocity shear between fast and slow solar streams may initiate the KH instability, is steady throughout the period under study $\pm 35^\circ$ from the heliographic equator (at $2.0-2.5~R_\odot$) as shown by the three panels of Figure 2.

In each of the 379 points of the solar corona where the UVCS relevant parameters have been obtained, the time series of the O VI $\lambda 1032$ variance $\mu_2(t)$ and O VI doublet intensity ratio $\rho(t)$ are used to compute the T-U Spearman's rank correlation r, which allows the assessment of monotonic relationships (whether linear or not) between two sample populations. It is defined as

$$r = \frac{\sum_{i=1}^{N} [R(\mu_{2}(t)) - \overline{R(\mu_{2}(t))}] \sum_{i=1}^{N} [R(\rho(t)) - \overline{R(\rho(t))}]}{\sqrt{\sum_{i=1}^{N} [R(\mu_{2}(t)) - \overline{R(\mu_{2}(t))}]^{2}} \sqrt{\sum_{i=1}^{N} [R(\rho(t)) - \overline{R(\rho(t))}]^{2}}},$$
(2)

where $R(\cdot)$ denotes the rank of the sorted data and the summation is extended to all N=379 points of the time series. The color-scale representation of the computed T-U Spearman's rank correlation r in the coronal locations observed with UVCS is shown in Figure 3(a), where the magnetic field dipole configuration by Banaszkiewicz et al. (1998) and the two-dimensional (2D) coronal electron density distribution by Guhathakurta et al. (1996), being representative of solar-minimum conditions, are also displayed.

Intriguingly, the larger T-U correlations are found at the edges of the polar coronal holes separating fast flows from the adjacent slower flows coming from the equatorial streamer regions, as expected. This is even clearer in Figure 3(b), where the Spearman's rank correlation r values found in the polar hole, equatorial streamer, and hole/streamer boundary regions (delimited in Figure 3(a) by red, blue, and green thicker magnetic field lines, respectively) are averaged in steps of $0.35~R_{\odot}$, from 1.4~ to $3.15~R_{\odot}$. That is, red, blue, and green symbols in Figure 3(b) correspond to fast wind, slow wind, and

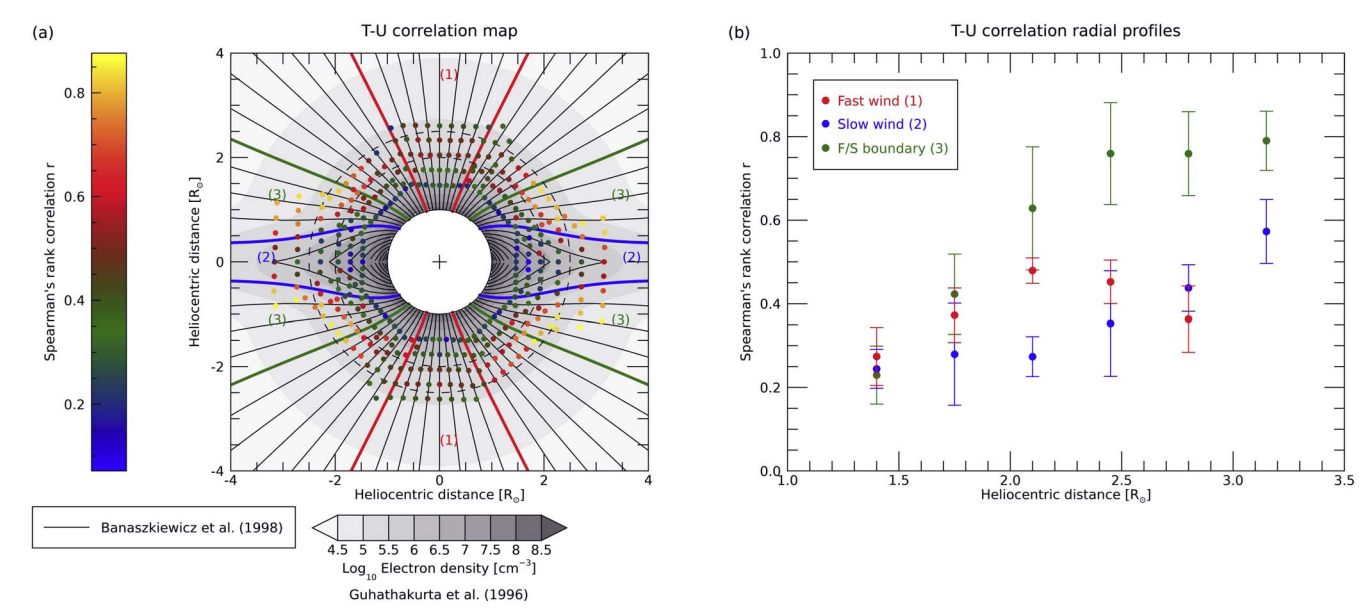


Figure 3. (a) Color-coded map of the Spearman's rank correlation r between the oxygen kinetic temperature T and the outflow speed U in the solar corona observed with UVCS. Overlaid are the magnetic field lines from the Banaszkiewicz et al. (1998) dipole model and (in tonalities of gray) isodensity curves from the Guhathakurta et al. (1996) solar-minimum coronal electron density distribution. Dashed—dotted circles at 2.0 and 2.5 R_{\odot} indicate the heliocentric range where the Carrington maps of Figure 2 were obtained. r values within polar hole, equatorial streamer, and hole/streamer boundary regions (delimited by red, blue, and green thicker magnetic field lines and marked as (1), (2), and (3), respectively) are averaged and displayed as radial profiles in panel (b), along with the corresponding standard deviation error bars.

fast/slow wind interaction regions, respectively. Within the open-field polar hole associated with the faster coronal wind (red circles), the T-U Spearman's correlation increases from low (0.27) at 1.4 R_{\odot} to moderate (0.48) at 2.1 R_{\odot} . Beyond this height, it decreases to 0.36 at 2.8 R_{\odot} . In the slower flows associated with closed magnetic field regions (blue circles), r remains low from 1.4 to 2.1 R_{\odot} with an average value of 0.27, after which it linearly increases to a moderate value of 0.57 at 3.15 R_{\odot} . Hence, interestingly, beyond 2.45 R_{\odot} the correlation between the temperature and the speed of the outflowing plasma is higher in the slow wind than in the polar wind. However, the highest T-U correlation is found along the boundary between open and closed magnetic field lines, where r monotonically increases up to a maximum value of about 0.76 at 2.45 R_{\odot} , flattening farther out. This observational evidence suggests that the differential flow of fast and slow wind along their boundary may initiate the KH instability. Indeed, KH vortices generated by the roll-up of the shear layer might then drive correlated fluctuations in T and U, according to the physical processes described in Section 1, detected with UVCS. Worth noting is the fact that, although lower close to the Sun, the Spearman's rank correlation r in the streamer regions tends to reach, at large heliocentric distances, the values observed at the boundary with the edges of the coronal holes (blue and green circles in Figure 3(b)). This can be easily interpreted in terms of the development of the KH instability, bearing in mind the magnetic morphology of the quiescent streamers. Initially diverging at the base of the solar atmosphere, the magnetic field lines converge farther out along the current sheet and toward the streamer cusp. This means that the coronal hole/streamer boundary is moving to lower latitude as the distance from the Sun increases. Therefore, the KH instability, which would arise at higher latitude closer to the Sun, is expected to be triggered by the shear flow at lower latitudes moving away from the Sun. Note that the T-Utemporal correlation could in principle be an effect of solar

rotation. Colder and slower streamer-related structures might indeed periodically protrude into the borders of hotter coronal holes, associated with faster flows, resulting in a trivial correlation. However, this possibility should be ruled out based on the great stability of the boundary layer between coronal hole edges and adjacent equatorial streamers during the minimum activity phase of solar cycle 22 (Figure 2). Furthermore, if solar rotation actually contributed to the observed correlation between temperature and velocity, then two populations should be observed in the scatter plot of μ_2 and ρ measured along the coronal hole/streamer discontinuity region, one related to the slow wind (at low μ_2 and ρ values) and another related to the fast wind (at higher μ_2 and ρ values). Instead, the $\mu_2 - \rho$ scatter plots along the velocity layer (not shown) exhibit only one clear and well-correlated population, confirming that the fluctuations in T and U are clearly due to some physical process, interpreted here as the KH instability.

In short, UVCS data seem to provide very promising clues in favor of a scenario in which the KH instability may play an important role in the plasma dynamics, as well as in the solar wind heating and acceleration at the interface between high-and low-speed coronal streams.

3. Nearly Incompressible MHD Theory for KH-driven Turbulence

In order to provide theoretical support for the results obtained in the previous section from the UVCS data analysis, coupled solar wind and nearly incompressible (NI) MHD turbulence transport equations have been solved with and without a shear source of turbulence included, to test whether or not the presence of a shear flow (associated with the onset of KH-excited turbulence) can lead to a higher correlation between coronal temperature and velocity fluctuations.

In the following, the KH instability is thus assumed to exist at the edges of coronal holes (based on the UVCS observational study that suggests its presence), introducing a distributed energy source term along the boundaries (i.e., a stream-shear source in the turbulence transport equations). It will be shown that, without changing the lower boundary conditions, the additional distributed energy source leads to an increased temperature-velocity correlation along the boundary relative to what might be expected in the core of the coronal hole where such a distributed energy source is absent. This section will thus quantify the statement that if a KH instability exists on the coronal hole boundaries, a higher plasma temperature-velocity correlation can be expected in those regions compared to other regions of the coronal hole, hence supporting the observational UVCS findings that have been interpreted here as due to a KH instability. To this end, the first step is to ascertain the critical speed that the shearing flow needs to have in order for a KH instability to develop. The characteristic speed in the sub-Alfvénic flow region is the slow magnetosonic mode speed $V_{\rm sm}$, which for the parallel field is $V_{\rm sm} = C_s$ (where C_s is the sound speed) and for the perpendicular field is $V_{\rm sm} = 0$. Depending on the orientation of the magnetic field relative to the tangential flows (largely unknown, but very likely not too aligned, at least locally, to the velocity shear owing to the presence of a complicated and quite disordered magnetic field topology), $0 \le V_{\rm sm} \le C_s$. The relevant characteristic speed in the super-Alfvénic flow is, on the other hand, the fast magnetosonic mode speed $V_{\rm fm}$, i.e., $V_{\rm fm} = (V_A^2 + C_s^2)^{1/2}$ and $V_{\rm fm} = V_{\rm A}$, for the perpendicular and parallel case, respectively (Miura & Pritchett 1982). The magnetosonic speeds are a function of $\cos^2(\theta)$; the ensemble average is thus $\langle \cos^2(\theta) \rangle =$ 1/2. Hence, the ensemble-averaged (squared) slow magnetosonic speed is $\langle V_{\rm sm}^2 \rangle = \frac{1}{2} C_s^2 (1 - \frac{\gamma}{4} \beta_p)$, with β_p the usual plasma beta, which is small for most of the regions under study, and γ the specific-heat ratio. Similarly, the ensemble-averaged expression of the fast magnetosonic speed is given by $\langle V_{\rm fm}^2 \rangle = V_{\rm A}^2 + \frac{1}{2} C_s^2 (1 + \frac{\gamma}{4} \beta_p)$, which in the small plasma beta limit means $\langle V_{\rm fm}^2 \rangle \sim V_{\rm A}^2$. Therefore, in the following, C_s and $V_{\rm A}$ are used as a critical speed in the stream-shear source term, in the sub- and super-Alfvénic flow, respectively.

The steady flow in a one-dimensional (1D) super-radially expanding open flux tube is assumed to be affected by shear-driven turbulence (Ruffolo et al. 2020) caused by the KH instability (DeForest et al. 2016; Yuan et al. 2019) at the interface between fast and slow solar wind. The cross-sectional area A(r) of the flux tube varies with the reciprocal of the magnetic field strength and can be expressed from the conservation equation of the magnetic field as

$$B_r A(r) = B_r r^2 f(r) = \text{const.}, \tag{3}$$

where $A(r) = r^2 f(r)$, and f(r), a super-radial expansion factor, is given by (Kopp & Holzer 1976)

$$f(r) = \frac{f_m \exp\left(\frac{r - r_a}{\sigma}\right) + 1 - (f_m - 1)\exp\left(\frac{R_{\odot} - r_a}{\sigma}\right)}{\exp\left(\frac{r - r_a}{\sigma}\right) + 1}, \quad (4)$$

with $f_m = 2$, $r_a = 2$ R_{\odot} , and $\sigma = 0.8$ R_{\odot} . The function f(r) is equal to 1 at r = 1 R_{\odot} and increases smoothly to the maximum value f_m over a long distance, with most of the change occurring, however, near the coronal base.

Considering the super-radial expansion, the steady flow can be described by the continuity equation, an inviscid momentum equation, and a pressure equation as

$$\frac{dn_s}{dr} = -\frac{2n_s}{r} - \frac{n_s}{U} \frac{dU}{dr} - \frac{n_s}{\sigma f(r)} \exp\left(\frac{r - r_a}{\sigma}\right) \times \frac{f_m - f(r)}{\exp\left(\frac{r - r_a}{\sigma}\right) + 1};$$
(5)

$$\rho_s U \frac{dU}{dr} = -\frac{dP}{dr} - \frac{GM_{\odot}}{r^2} \rho_s; \tag{6}$$

$$\frac{dP}{dr} = -\frac{\gamma P}{U} \frac{dU}{dr} - \frac{2\gamma P}{r} - \frac{\gamma P}{\sigma f(r)} \exp\left(\frac{r - r_a}{\sigma}\right) \\
\times \frac{f_m - f(r)}{\exp\left(\frac{r - r_a}{\sigma}\right) + 1} + (\gamma - 1)s_1 \frac{S_t}{U}, \tag{7}$$

where $n_s(\rho_s)$ is the solar wind number (mass) density, U the solar wind speed, P the thermal pressure, G the gravitational constant, M_{\odot} the solar mass, S_t the turbulent heating term for protons, s_1 the fraction of turbulence energy that heats the thermal coronal plasma, and $\gamma = 5/3$ a polytropic index. It is assumed that $s_1 = 0.6$, which means that 60% of the turbulent energy heats the coronal plasma (Breech et al. 2009; Cranmer et al. 2009; Engelbrecht & Strauss 2018; Chhiber et al. 2019; Adhikari et al. 2021). Some fraction of the turbulence energy may produce a nonthermal ion population (possibly due to stochastic acceleration by magnetic islands; e.g., Zank et al. 2014; Zhao et al. 2018; Adhikari et al. 2019; Zhao et al. 2019), and some fraction generates a nonthermal electron population. Similarly, some fraction of the turbulence energy may heat the heavier ion population, such as O⁺⁵ ions. The transport equation for the O⁺⁵ temperature is here derived by considering that the oxygen ions can be heated by the same heating process as solar wind protons. The 1D steady-state transport equation for the temperature of O⁺⁵ ions can be obtained by using $P_0 = 2n_0k_BT_0$ (where P_0 , n_0 , and T_0 are the pressure, density, and temperature of the heavier O⁺⁵ ions, respectively) in Equation (7) as

$$\frac{dT_0}{dr} = -2(\gamma - 1)\frac{T_0}{r} - (\gamma - 1)\frac{T_0}{U}\frac{dU}{dr} - (\gamma - 1)\frac{T_0}{\sigma f(r)}\exp\left(\frac{r - r_a}{\sigma}\right)\frac{f_m - f(r)}{\exp\left(\frac{r - r_a}{\sigma}\right) + 1} + \frac{(\gamma - 1)s_2S_0}{2k_BUn_0}.$$
(8)

The O^{+5} ions are assumed to be advected by the bulk solar wind speed. In Equation (8), the last term on the right-hand side is the heating term caused by the dissipation of turbulence. The parameter S_0 is the turbulent heating term for O^{+5} ions, and $s_2 = 0.2$ is the fraction of turbulence energy heating the O^{+5} ions. As the mass of the O^{+5} ions is 16 times heavier than the proton mass, the heating term S_0 for O^{+5} ions is higher than that of protons S_t . The third term on the right-hand side of Equations (5), (7), and (8) is due to the super-radial expansion factor (see Kopp & Holzer 1976; Suzuki & Inutsuka 2005,

2006), which disappears when $A(r) = r^2$ (e.g., Usmanov et al. 2018; Chhiber et al. 2019; Adhikari et al. 2020). Equations (6) and (7) yield

$$\frac{C_s^2}{U^2}(M_s^2 - 1)\frac{dU}{dr} = \frac{2\gamma P}{\rho_s U r} - (\gamma - 1)s_1 \alpha \frac{S_t}{m_p n_s U^2} - \frac{GM_{\odot}}{U r^2} + \frac{\gamma P}{\sigma f(r)\rho_s U} \exp\left(\frac{r - r_a}{\sigma}\right) \frac{f_m - f(r)}{\exp\left(\frac{r - r_a}{\sigma}\right) + 1}, \quad (9)$$

where $M_s = U/C_s$ is the sonic Mach number and $C_s^2 = \gamma P/\rho_s$ is the square of the sound speed. Equation (8) is not used when deriving Equation (9) because the temperature T_0 of the O^{+5} ions, being the minority species, does not react on the flow. Again, the last term on the right-hand side of Equation (9) corresponds to the super-radial expansion factor. Equation (9) possesses a sonic point when $M_s = 1$ or $U = C_s$. L'Hôpital's rule is used to solve Equation (9) in the vicinity of the sonic point, as in Adhikari et al. (2020). This model only includes a thermal force, denoted by the first term on the right-hand side of Equation (6), as the main driving force of the solar wind, and the ponderomotive force is not included (see Holzer & Axford 1970; Leer et al. 1982; Withbroe 1988; Fisk et al. 1999; Cranmer & van Ballegooijen 2010; Verdini et al. 2010; Cranmer et al. 2013), nor is the wave pressure (McKenzie et al. 1995). The thermal force is produced by the hot coronal plasma of $\sim 10^6$ K, which is caused by the dissipation of turbulence energy. The turbulent heating term for protons and oxygen ions $S_{t(0)}$ can be derived from a von Kármán phenomenology and is given by (Verdini et al. 2010; Zank et al. 2018b)

$$S_{t(0)} = \alpha m_{p(0)} n_{s(0)} \left[2 \frac{\langle z^{\infty+2} \rangle^2 \langle z^{\infty-2} \rangle^{1/2}}{L_{\infty}^+} + 2 \frac{\langle z^{\infty-2} \rangle^2 \langle z^{\infty+2} \rangle^{1/2}}{L_{\infty}^-} + E_D^{\infty} \times \left(\frac{\langle z^{\infty+2} \rangle^{1/2}}{\lambda_{\infty}^-} + \frac{\langle z^{\infty-2} \rangle^{1/2}}{\lambda_{\infty}^+} \right) + 2 \frac{\langle z^{\infty+2} \rangle \langle z^{\infty+2} \rangle \langle z^{\infty-2} \rangle^{1/2}}{L_{\infty}^+} \right], \tag{10}$$

where $\alpha=0.14$ is a von Kármán–Taylor constant, which also determines the turbulent heating rate; m_p is the proton mass; and $m_0=16m_p$ is the oxygen mass. The parameters $\langle z^{\infty\pm2} \rangle$ are the quasi-2D energy in forward- and backward-propagating modes (\mathbf{z}^{\pm} being the fluctuating Elsässer variables; Elsässer 1950), and L_{∞}^{\pm} are the corresponding correlation functions. The parameter E_D^{∞} is the quasi-2D residual energy, and $\langle z^{*+2} \rangle$ is the NI slab energy in forward-propagating modes. In Equation (10), the first three terms inside the square brackets are the heating rates associated with quasi-2D turbulence, and the last term corresponds to a minority NI/slab turbulence.

The 1D steady-state transport equations for the majority quasi-2D turbulence, including the super-radial expansion factor, are given by (Zank et al. 2017, 2018a; Adhikari et al. 2017, 2020)

$$U\frac{d\langle z^{\infty\pm2}\rangle}{dr} = -\left[\frac{\langle z^{\infty\pm2}\rangle}{2} + \left(2a - \frac{1}{2}\right)E_{D}^{\infty}\right]\frac{dU}{dr}$$

$$-\frac{2U}{r}\left[\frac{\langle z^{\infty\pm2}\rangle}{2} + \left(2a - \frac{1}{2}\right)E_{D}^{\infty}\right] - \frac{U}{\sigma f(r)}\left[\frac{\langle z^{\infty\pm2}\rangle}{2} + \left(2a - \frac{1}{2}\right)E_{D}^{\infty}\right] - \frac{U}{\sigma f(r)}\left[\frac{\langle z^{\infty\pm2}\rangle}{2} + \left(2a - \frac{1}{2}\right)E_{D}^{\infty}\right]\exp\left(\frac{r - r_{a}}{\sigma}\right)\frac{f_{m} - f(r)}{\exp\left(\frac{r - r_{a}}{\sigma}\right) + 1}$$

$$-2\alpha\frac{\langle z^{\infty\pm2}\rangle\langle z^{\infty\mp2}\rangle^{1/2}}{\lambda_{\infty}^{\pm}} + S^{\langle z^{\infty\pm2}\rangle};$$

$$(11)$$

$$U\frac{dE_{D}^{\infty}}{dr} = -\left[\frac{E_{D}^{\infty}}{2} + \left(2a - \frac{1}{2}\right)E_{T}^{\infty}\right] - \frac{U}{\sigma f(r)}\left[\frac{E_{D}^{\infty}}{2} + \left(2a - \frac{1}{2}\right)E_{T}^{\infty}\right] - \frac{U}{\sigma f(r)}\left[\frac{E_{D}^{\infty}}{2} + \left(2a - \frac{1}{2}\right)E_{T}^{\infty}\right] + S^{E_{D}^{\infty}};$$

$$-\alpha E_{D}^{\infty}\left(\frac{\langle z^{\infty+2}\rangle^{1/2}}{\lambda_{\infty}^{-}} + \frac{\langle z^{\infty-2}\rangle^{1/2}}{\lambda_{\infty}^{+}}\right) + S^{E_{D}^{\infty}};$$

$$U\frac{dL_{\infty}^{\pm}}{dr} = -\left[\frac{L_{\infty}^{\pm}}{2} + \left(a - \frac{1}{4}\right)L_{D}^{\infty}\right] - \frac{U}{\sigma f(r)}\left[\frac{L_{\infty}^{\pm}}{2} + \left(a - \frac{1}{4}\right)L_{D}^{\infty}\right]$$

$$\times \exp\left(\frac{r - r_{a}}{\sigma}\right)\frac{f_{m} - f(r)}{\exp\left(\frac{r - r_{a}}{\sigma}\right) + 1};$$

$$U\frac{dL_{D}^{\infty}}{dr} = -\left[\frac{L_{D}^{\infty}}{2} + \left(2a - \frac{1}{2}\right)(L_{\infty}^{+} + L_{\infty}^{-})\right]\frac{dU}{dr}$$

$$-\frac{2U}{r}\left[\frac{L_{D}^{\infty}}{2} + \left(2a - \frac{1}{2}\right)(L_{\infty}^{+} + L_{\infty}^{-})\right] - \frac{U}{\sigma f(r)}$$

$$\times \left[\frac{L_{D}^{\infty}}{2} + \left(2a - \frac{1}{2}\right)(L_{\infty}^{+} + L_{\infty}^{-})\right]$$

$$\times \exp\left(\frac{r - r_{a}}{\sigma}\right)\frac{f_{m} - f(r)}{\exp\left(\frac{r - r_{a}}{\sigma}\right)} + 1,$$
(14)

where L_D^∞ is the quasi-2D correlation function for the residual energy and E_T^∞ is the quasi-2D total turbulence energy. The third term on the right-hand side of Equations (11)–(14) is due to the inclusion of the super-radial expansion factor, which makes these equations different from the quasi-2D turbulence transport equations of Adhikari et al. (2020). The term "S" refers to the turbulent shear source for the energy in forward-and backward-propagating modes and the residual energy generated by KH instability formed at the interface between the fast and slow solar wind streams below the Alfvén surface, as discussed below.

The 1D steady-state transport equations for the energy in NI/slab forward-propagating modes and the corresponding correlation function are given by (Zank et al. 2017, 2018a; Adhikari et al. 2017, 2020)

$$(U - V_{A}) \frac{d\langle z^{*+2} \rangle}{dr} = -\frac{1}{2} \frac{dU}{dr} \left\langle z^{*+2} \right\rangle + (2b - 1) \frac{U}{r} \left\langle z^{*+2} \right\rangle$$

$$+ \frac{V_{A}}{2\rho_{s}} \frac{d\rho_{s}}{dr} \left\langle z^{*+2} \right\rangle + \frac{1}{2} (2b - 1) \frac{U\langle z^{*+2} \rangle}{\sigma f(r)}$$

$$\times \exp\left(\frac{r - r_{a}}{\sigma}\right) \frac{f_{m} - f(r)}{\exp\left(\frac{r - r_{a}}{\sigma}\right) + 1}$$

$$- 2\alpha \frac{\langle z^{*+2} \rangle \langle z^{\infty-2} \rangle^{1/2}}{\lambda_{\infty}^{+}} + S^{\langle z^{*+2} \rangle};$$

$$(U - V_{A}) \frac{dL_{*}^{+}}{dr} = -\frac{1}{2} \frac{dU}{dr} L_{*}^{+} + (2b - 1) \frac{U}{r} L_{*}^{+}$$

$$(15)$$

$$(U - V_{A}) \frac{dL_{*}^{+}}{dr} = -\frac{1}{2} \frac{dU}{dr} L_{*}^{+} + (2b - 1) \frac{U}{r} L_{*}^{+} + \frac{V_{A}}{2\rho_{s}} \frac{d\rho_{s}}{dr} L_{*}^{+} + \frac{1}{2} (2b - 1) \frac{UL_{*}^{+}}{\sigma f(r)} \times \exp\left(\frac{r - r_{a}}{\sigma}\right) \frac{f_{m} - f(r)}{\exp\left(\frac{r - r_{a}}{\sigma}\right) + 1}.$$
 (16)

Again, the fourth term on the right-hand side of Equations (15) and (16) is due to the super-radial expansion. The parameter $V_{\rm A} = (B_0/\sqrt{\mu_0 \rho_s}) \cdot (r_0/r)^2 \cdot (1/f(r))$, where B_0 is the magnetic field at a reference point r_0 and μ_0 is the magnetic permeability, is the Alfvén velocity. In Equations (15) and (16), b = 0.26 is used (see Zank et al. 2012, 2017, for further discussion). The parameter $S^{\langle z^{*+2} \rangle}$ denotes the turbulent shear source for the energy in NI/slab forward-propagating modes. Equations (15) and (16) are derived by assuming the normalized cross-helicity $\sigma_c^* = 1$ and the normalized residual energy $\sigma_D^* = 0$ (Zank et al. 2017; Adhikari et al. 2020). This is the condition observed at highly field-aligned flows, i.e., unidirectional Alfvén waves (Telloni et al. 2019a; Zhao et al. 2020). Such flows exhibit a Kolmogorov-type power law (Telloni et al. 2019a; Zank et al. 2020; Zhao et al. 2020). Equations (11)–(16) are thus a set of turbulence transport equations describing the evolution of turbulence in highly fieldaligned flows (see Adhikari et al. 2020, for detailed discussion).

It will be important in the future to determine whether there is an in situ source of turbulence in the quite solar corona, which complements the generation of turbulence at the coronal base (Zank et al. 2018a). In the super-Alfvénic solar wind, the generation of stream-shear and pickup ions has been identified as an important source of turbulence (Zank et al. 1996; Smith et al. 2006; Breech et al. 2008; Adhikari et al. 2014; Zank et al. 2018b). It is not completely known at what distance the shear source of turbulence arises (e.g., Ruffolo et al. 2020). The possibility that there may be a shear source of turbulence produced by the KH instability formed at the interface between the fast and slow solar wind streams is considered here. In situ measurements acquired with Parker Solar Probe (Fox et al. 2016), which will soon fly inside the solar corona below the Alfvén surface, will clarify whether sources of turbulence exist within coronal holes or not.

In deriving the expression for the turbulent shear source "S," the dimensional argument of Zank et al. (2017) has been adopted, recognizing that, as argued above, the characteristic speed in the region below the Alfvén surface is the sound speed

Parameters	Case I (black)	Case II (blue)	Case III (red)
$\langle z^{\infty+2} \rangle \text{ (km}^2 \text{ s}^{-2})$	6.5×10^{5}	6×10^{5}	5.5×10^{5}
$\langle z^{\infty-2} \rangle \text{ (km}^2 \text{ s}^{-2})$	6.5×10^{5}	6×10^{5}	5.5×10^{5}
$E_D^{\infty} (\mathrm{km}^2 \mathrm{s}^{-2})$	2000	2000	2000
$L_{\infty}^{+} (\mathrm{km}^{3} \mathrm{s}^{-2})$	5.2×10^{10}	4.8×10^{10}	4.4×10^{10}
$L_{\infty}^{-} (\mathrm{km}^{3} \mathrm{s}^{-2})$	5.2×10^{10}	4.8×10^{10}	4.4×10^{10}
L_D^{∞} (km ³ s ⁻²)	1.6×10^{8}	1.6×10^{8}	1.6×10^{8}
$\langle z^{*+2} \rangle \text{ (km}^2 \text{ s}^{-2})$	1100	1100	1100
$L_{*}^{+} \text{ (km}^3 \text{ s}^{-2}\text{)}$	1.76×10^{8}	1.76×10^{8}	1.76×10^{8}
$U (\mathrm{km \ s}^{-1})$	16.69	16.37	16.05
$n (\mathrm{cm}^{-3})$	10^{7}	10^{7}	10^{7}
T(K)	5×10^{5}	5×10^{5}	5×10^{5}
T_0 (K)	1.4×10^{7}	1.4×10^{7}	1.4×10^{7}

 C_s . In this case, the shear source of turbulence can be written in the form

$$S_{\langle z^{\infty}, *\pm^{2} \rangle}^{s} = C_{\infty, *}^{s+} \frac{r_{0}^{s} |\Delta U| C_{s}^{2}}{r^{2}} = \gamma C_{\infty, *}^{s+} \frac{r_{0}^{s} |U - U_{0}^{s'}| P}{\rho_{s} r^{2}};$$

$$S_{\langle z^{\infty-2} \rangle}^{s} = C_{\infty}^{s-} \frac{r_{0}^{s} |\Delta U| C_{s}^{2}}{r^{2}} = \gamma C_{\infty}^{s-} \frac{r_{0}^{s} |U - U_{0}^{s'}| P}{\rho_{s} r^{2}};$$

$$S_{E_{D}^{\infty}}^{s} = C_{\infty}^{sE_{D}} \frac{r_{0}^{s} |\Delta U| C_{s}^{2}}{r^{2}} = \gamma C_{\infty}^{sE_{D}} \frac{r_{0}^{s} |U - U_{0}^{s'}| P}{\rho_{s} r^{2}},$$

$$(17)$$

where $U_0^{s'}$ is the subsonic solar wind speed in the slow wind region of the sheared flow, r_0^s denotes the position above the sonic surface, and $C_{\infty,*}^{s\pm,E_p}$ denotes the strength of the shear source of turbulence. $\Delta U = |U - U_0^{s'}|$ and $C_s^2 = \gamma P/\rho_s$ are used: this illustrates that the shear source of turbulence does not depend only on r, as in Zank et al. (2017), Zank et al. (2018a), and Adhikari et al. (2017), but also on the solar wind speed U, the thermal pressure P, and the proton mass density ρ_s . Three different boundary conditions have been used: case I, $r_0^s = 1.39$ R_{\odot} and $U_0^{s'} = 286.13$ km s⁻¹; case II, $r_0^s = 1.45$ R_{\odot} and $U_0^{s'} = 274.19$ km s⁻¹; case III, $r_0^s = 1.52$ R_{\odot} and $U_0^{s'} = 260.58$ km s⁻¹

Similarly, by recognizing that the characteristic speed above the Alfvén surface is the Alfvén velocity, the shear source of turbulence in this region can be written in the form

$$S_{\langle z^{\infty}, *\pm 2 \rangle}^{A} = C_{\infty, *}^{a + \frac{r_{0}^{a} \mid \Delta U \mid V_{A}^{2}}{r^{2}}} = C_{\infty, *}^{a + \frac{r_{0}^{a} \mid U - U_{0}^{a'} \mid V_{A}^{2}}{r^{2}};$$

$$S_{\langle z^{\infty - 2} \rangle}^{A} = C_{\infty}^{a - \frac{r_{0}^{a} \mid \Delta U \mid V_{A0}^{2}}{r^{2}}} = C_{\infty}^{a - \frac{r_{0}^{a} \mid U - U_{0}^{a'} \mid V_{A}^{2}}{r^{2}};$$

$$S_{E_{D}^{\alpha}}^{A} = C_{\infty}^{aE_{D}} \frac{r_{0}^{a} \mid \Delta U \mid V_{A0}^{2}}{r^{2}} = C_{\infty}^{aE_{D}} \frac{r_{0}^{a} \mid U - U_{0}^{a'} \mid V_{A}^{2}}{r^{2}},$$
(18)

where $\Delta U = |U - U_0^{a'}|$ is used. The parameter $U_0^{a'}$ is the sub-Alfvénic solar wind speed in the slow wind region of the sheared flow, r_0^a denotes the position of the Alfvén surface, and $C_{\infty,*}^{a\pm E_D}$ denotes the strength of the shear source of turbulence. Equation (18) shows that the turbulent shear source above the Alfvén surface depends on the heliocentric distance r, the solar wind speed U, and the Alfvén velocity V_A . The following

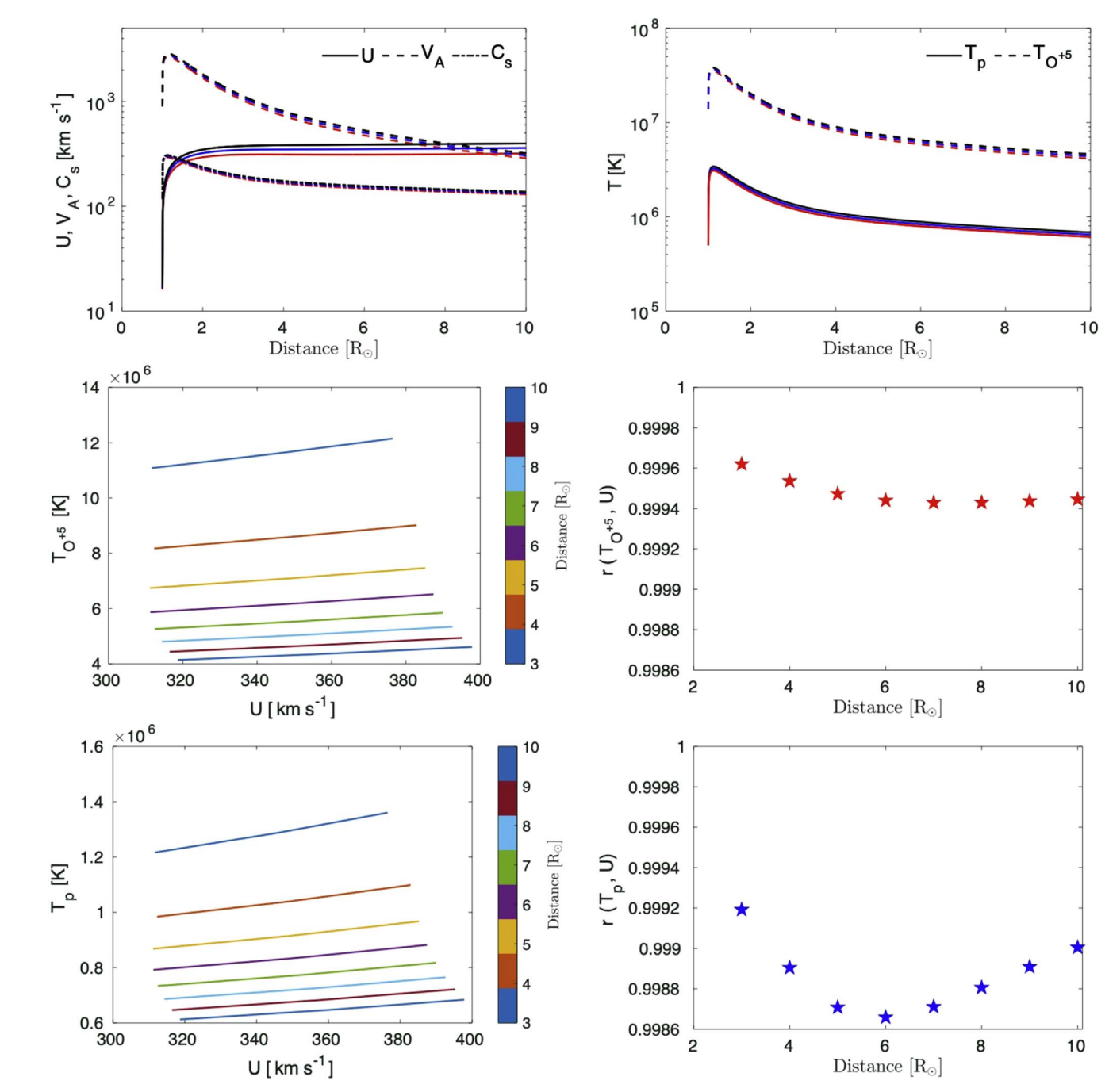


Figure 4. Top left: solar wind speed (solid curve), Alfvén velocity (dashed curve), and sound speed (dashed—dotted—dashed curve) as a function of heliocentric distance. Top right: solar wind proton temperature (solid curve) and O⁺⁵ temperature (dashed curve) as a function of heliocentric distance. Middle panels: relationship (left) and correlation (right) between the oxygen temperature and the solar wind speed at different distances. Bottom panels: same as the middle panels, but for protons. Black, blue, and red curves in the top panels correspond to the different boundary conditions as listed in Table 1. The turbulent shear source is not included.

values for r_0^a and $U_0^{a'}$ are used for three different cases: case I, $r_0^a = 7.98~R_\odot$ and $U_0^{a'} = 406.10~{\rm km~s^{-1}}$; case II, $r_0^a = 8.37~R_\odot$ and $U_0^{a'} = 368.74~{\rm km~s^{-1}}$; case III, $r_0^a = 8.91~R_\odot$ and $U_0^{a'} = 326.84~{\rm km~s^{-1}}$.

For the three cases shown in Table 1, a Runge–Kutta fourth-order method has been used to solve the coupled solar wind and turbulence transport Equations (5)–(16), from 1 to $10 R_{\odot}$.

The coupled transport equations have been solved first without and then with the shear source of turbulence. In the context of NI MHD turbulence, quasi-2D turbulence is mainly responsible for the heating of the coronal plasma and the

driving of the solar wind (Zank et al. 2018a; Adhikari et al. 2020). In this work, it is assumed that the quasi-2D energy in forward-propagating modes at the coronal base in case I is 1.08 and 1.18 times greater than those in cases II and III, respectively, and that in case II is 1.09 times greater than that in case III. Therefore, case I (III) contains the largest (smallest) quasi-2D turbulence energy.

Consider first the case without a shear source of turbulence, shown in Figure 4. The solar wind speed (top left panel) in case I (black curve) accelerates to a larger value more rapidly than in cases II and III (blue and red curves, respectively), the solar wind of case III (red curve) being the slowest. The Alfvén

Table 2
Strengths of the KH-induced Shear Driving Turbulence for Quasi-2D and Slab Turbulence in the Regions below and above the Alfvén Surface, Denoted by the Superscript s and a, Respectively

Parameters	Case I (black)	Case II (blue)	Case III (red)
$\overline{C_{\infty}^{s+}}$	2.8	2.8	2.8
C_{∞}^{s-}	2.8	2.8	2.8
$C_{\infty}^{sE_D}$	-0.1	-0.1	-0.1
C_*^{s+}	2.8	2.8	2.8
C_{∞}^{a+}	2	2	2
C_{∞}^{a-}	2	2	2
C_{∞}^{s+} C_{∞}^{s-} C_{∞}^{s-} $C_{\infty}^{sE_D}$ C_{∞}^{s+} C_{∞}^{s+} C_{∞}^{a+} C_{∞}^{a-} $C_{\infty}^{aE_D}$ C_{∞}^{a+}	-0.1	-0.1	-0.1
C_*^{a+}	2	2	2

velocity (dashed curve) and the sound speed (dashed—dotted—dashed curve) increase to peak values and decrease with increasing heliocentric distance thereafter. Similar to the solar wind speed, the Alfvén velocity and the sound speed in case I (dashed and dashed—dotted—dashed black curves, respectively) are greater than those in cases II and III (dashed and dashed—dotted—dashed blue and red curves, respectively).

The top right panel of Figure 4 shows that the solar wind O⁺⁵ and proton temperatures (dashed and solid curve, respectively) increase rapidly to peak values near the base of the solar corona and then decrease gradually with increasing heliocentric distance. Because the oxygen mass is larger than that of protons, the temperature of O⁺⁵ ions is greater than the proton temperature as a function of heliocentric distance. Similar to the solar wind speed, the O⁺⁵ and proton temperatures are highest in case I (black curves) and lowest in case III (red curves) with increasing heliocentric distance. Both oxygen and proton temperatures follow similar radial profiles because the heating mechanism is assumed to be the same.

Considering that the O⁺⁵ ions are advected by the solar wind speed, the relationship between O⁺⁵ temperature and solar wind speed can be calculated. To this end, the three different values of U and T (i.e., due to the three different boundary conditions) are derived from the black, blue, and red curves in the top left and top right panels of Figure 4 at heliocentric distances of 2, 4, 5, 6, 7, 8, 9, and 10 R_{\odot} . The middle left panel of Figure 4 shows that the O⁺⁵ temperature increases linearly with the solar wind speed. As shown in the middle right panel of the same figure, the oxygen T-U correlation is very high, although this decreases slightly with increasing heliocentric distance in the absence of a KH-driven source of turbulence. It is worth noting here that the displayed T-U correlation is not strictly a temporal correlation, as is the one estimated in the previous section based on long time series of UVCS measurements. Rather, it is a functional relationship obtained by considering different solutions of the MHD coronal model using different boundary conditions. However, assuming that the different boundary conditions mimic temporal fluctuations of the coronal plasma properties, then this plot can be compared, at least qualitatively, to Figure 3(b).

As with the O⁺⁵ ions, the bottom panels of Figure 4 show the relationship between the solar wind proton temperature and bulk speed (left), and the correlation between them (right) as a function of heliocentric distance, based on the three different solutions for the modeled corona displayed in the top panels. As expected, the results corresponding to protons are very

similar to those obtained for the oxygen component of the solar wind.

Consider now a KH-driven source of turbulence, augmenting the model equations with the source terms of Equations (17) and (18). Using the parameter values shown in Table 2, the coupled solar wind and turbulence transport equations with the turbulent shear source included are solved from the base of the solar corona up to $10~R_{\odot}$, for increasing strengths of the shear-driven turbulence. The theoretical solutions of the solar wind speed, sound speed, Alfvén velocity, and proton and oxygen temperatures as a function of heliocentric distance are shown in the top panels of Figure 5.

With the shear source of turbulence included, the solar wind speed, Alfvén velocity, and sound speed (top left panel of Figure 5) increase to higher values moving away from the Sun compared to the case where the turbulent shear source is not present. Similarly, the O⁺⁵ and proton temperatures decrease more slowly with increasing heliocentric distance than those without the turbulent shear source (top right panel of Figure 5).

In the presence of a turbulent shear source, the O^{+5} and proton temperatures are also linearly related to the solar wind speed (middle left and bottom left panels of Figure 5, respectively), and their correlations are very high. However, unlike the case without the shear source of turbulence, the result clearly shows that a turbulent shear source leads the T-U correlation for both the oxygen and the proton component of the solar wind to increase with distance (middle right and bottom right panels of Figure 5, respectively). It turns out that the stronger the shear source of turbulence, the higher the temperature and the velocity, and the higher their correlation. This is consistent with observations described above (Figure 3(b)), supporting the idea that the shear-driven KH instability may underlie the observed T-U correlation along the streamer boundaries.

The numerical results presented in this section allow the following interpretation to be drawn. In modeled open-field regions, everything decreases naturally since there is no instability or source of turbulence. However, along the flanks of streamer regions bordering the coronal hole edges, a KH instability may be generated owing to velocity shear between the fast and slow solar wind. If this process is continuous, then this drives turbulence in the hole/streamer boundary region continuously. The KH-generated turbulent shear source will input energy into the system. Thus, the more turbulence energy available, the more this energy will heat and accelerate the coronal plasma, which then becomes hotter and faster. The increase in temperature and velocity, as well as in their correlation, in the presence of turbulent shear sources hints that the KH instability may be at work. It is true that there exists a (high) correlation between T and U also when the turbulent shear source is not present, but this follows naturally from the thermodynamics of the solar corona. That is, if the plasma temperature is very large, it will produce a large pressure gradient that is responsible for driving the solar wind. Thus, it is not surprising that a high T-U correlation is observed even in the absence of a shear source of turbulence. Also, as expected, the absolute values of the observed and theoretical T-U correlations are different because, unlike modeling data, remote-sensing observations are affected by both physical and instrumental noise and by issues related to integration along the line of sight, all of which tend to lower the correlation level with respect to that obtained from numerical calculations in

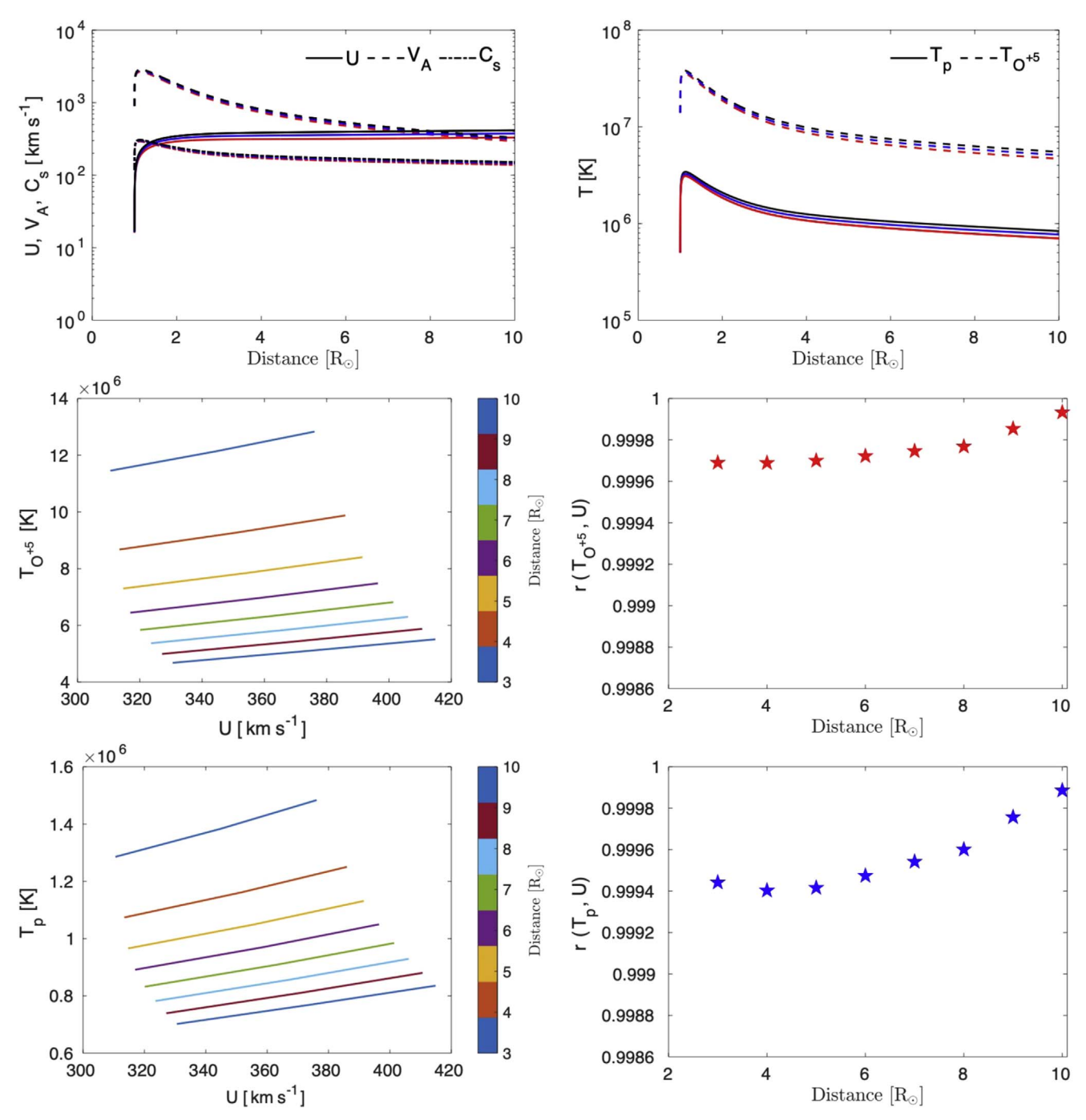


Figure 5. Same as Figure 4, but now including a KH-driven turbulent shear source in the turbulence transport equations.

which these sources of noise are neglected. However, the key points worthy of attention here are threefold: (i) the correlation between temperature and velocity decreases slightly with distance without turbulent shear source, while the $T\!-\!U$ correlation is larger and furthermore increases with distance in the presence of a shear source of turbulence; (ii) the solar wind temperature decreases more slowly and the solar wind speed increases more quickly with increasing heliocentric distance when including the shear source of turbulence; (iii) the correlation between T and U is proportional to the strength of the shear source of turbulence. It follows that something (here interpreted as due to the generation of a KH instability) must be changing the physical temperature conditions on the boundary

versus elsewhere in the coronal hole, causing T and U to be more correlated. These numerical results indeed indicate that a KH-driven shear source of turbulence enhances the correlation between the solar wind speed and temperature, thus corroborating the observational evidence outlined in the previous section and explained in terms of a KH instability initiated at the boundary layer between high- and low-speed coronal streams.

4. Concluding Remarks

Possible evidence, from both an observational and theoretical perspective, for the onset of the KH instability at the interface between fast and slow coronal flows has been

provided in this paper for the first time. By exploiting long time series of UVCS spectroscopic measurements of the UV corona encompassing 15 months during solar minimum of solar cycle 22, the level of correlation between the oxygen kinetic temperature T and outflow speed U fluctuations is studied over the entire 360° corona from 1.4 to 3.3 R_{\odot} . The highest values are found at the discontinuity layer at the edges of the coronal holes forming the boundaries of the adjacent streamers and interpreted as manifestations of KH-induced roll-up of the shear layer. Indeed, the formation of KH vortices drives significant heating and subsequent acceleration of the coronal plasma, thus leading to a simultaneous increase in coronal temperature T and radial velocity U. Along the boundary layer between coronal wind flows with different velocities, the continuous pattern of KH ripples interspersed with smooth, unperturbed regions of the shear flow, typical of a welldeveloped KH instability, can thus be revealed in UVCS data as well-correlated fluctuations in temperature and velocity. This picture is supported by a shear-driven NI MHD turbulence 1D analysis. A KH-driven shear source of turbulence is indeed shown to induce additional energy deposition to the coronal plasma, which is thus further accelerated to higher velocities. Furthermore, the shear-driven enhancement in T and U results in a higher and increasing degree of correlation along the boundary layer compared to the case without the KH instability. Thus, although the enhanced flow-heating correlation along the hole/streamer interface could also result from other different mechanisms, such as reconnection, waves, small-scale turbulence dissipation, and a mixture of different flow tube physical parameters, which therefore cannot be ruled out "a priori," the KH instability represents a viable mechanism for both mediating dynamical stream-stream interaction between the slow and the fast wind and transferring energy to the the coronal plasma.

The detection of large-scale, shear-driven KH instability in the inhomogeneous flow of the solar corona and its role in the 1 million degree coronal plasma heating are important and critical questions that the Metis coronagraph on board Solar Orbiter can address. Metis will observe the solar corona more closely than ever before in space exploration (during the first close approach to the Sun, in early 2022, Solar Orbiter will be as close as 0.32 au). By imaging the solar coronal simultaneously in polarized brightness and in H I Ly α ultraviolet light, from an unprecedented vantage point, Metis will have the unique opportunity to resolve KH vortex-like structures (as well as any other spatial perturbations) in the coronal regions characterized by stream —stream dynamic phenomena.

D.T. was partially supported by the Italian Space Agency (ASI) under contract 2018-30-HH.0. L.A. and G.P.Z. acknowledge the partial support of a NASA Parker Solar Probe contract SV4-84017, an NSF EPSCoR RII-Track-1 Cooperative Agreement OIA-1655280, and a NASA IMAP grant through SUB000313/80GSFC19C0027. L.S.-V. was supported by Swedish National Space Agency (SNSA) grants 86/20 and 145/18.

Facility: SOHO (UVCS).

Software: DAS (https://lweb.cfa.harvard.edu/uvcs/).

ORCID iDs

Daniele Telloni https://orcid.org/0000-0002-6710-8142 Laxman Adhikari https://orcid.org/0000-0003-1549-5256

```
Gary P. Zank https://orcid.org/0000-0002-4642-6192
Lingling Zhao https://orcid.org/0000-0002-4299-0490
Luca Sorriso-Valvo https://orcid.org/0000-0002-5981-7758
Ester Antonucci https://orcid.org/0000-0003-4155-6542
Silvio Giordano https://orcid.org/0000-0002-3468-8566
Salvatore Mancuso https://orcid.org/0000-0002-9874-2234
```

References

Abbo, L., Antonucci, E., Mikić, Z., et al. 2010, AdSpR, 46, 1400

```
Abbo, L., Ofman, L., Antiochos, S. K., et al. 2016, SSRv, 201, 55
Adhikari, L., Khabarova, O., Zank, G. P., & Zhao, L.-L. 2019, ApJ, 873, 72
Adhikari, L., Zank, G. P., Hu, Q., & Dosch, A. 2014, ApJ, 793, 52
Adhikari, L., Zank, G. P., Hunana, P., et al. 2017, ApJ, 841, 85
Adhikari, L., Zank, G. P., & Zhao, L.-L. 2020, ApJ, 901, 102
Adhikari, L., Zank, G. P., Zhao, L.-L., Nakanotani, M., & Tasnim, S. 2021,
   A&A, 650, A16
Antonucci, E. 2006, SSRv, 124, 35
Antonucci, E., Abbo, L., & Dodero, M. A. 2005, A&A, 435, 699
Antonucci, E., Abbo, L., & Telloni, D. 2012, SSRv, 172, 5
Antonucci, E., Dodero, M. A., & Giordano, S. 2000, SoPh, 197, 115
Antonucci, E., Harra, L., Susino, R., & Telloni, D. 2020a, SSRv, 216, 117
Antonucci, E., Romoli, M., Andretta, V., et al. 2020b, A&A, 642, A10
Banaszkiewicz, M., Axford, W. I., & McKenzie, J. F. 1998, A&A, 337, 940
Berger, T. E., Slater, G., Hurlburt, N., et al. 2010, ApJ, 716, 1288
Breech, B., Matthaeus, W. H., Cranmer, S. R., Kasper, J. C., & Oughton, S.
   2009, JGRA, 114, A09103
Breech, B., Matthaeus, W. H., Minnie, J., et al. 2008, JGRA, 113, A08105
Brueckner, G. E., Howard, R. A., Koomen, M. J., et al. 1995, SoPh, 162,
Chandrasekhar, S. 1961, International Series of Monographs on Physics
   (Oxford: Clarendon), 1961
Chhiber, R., Usmanov, A. V., Matthaeus, W. H., Parashar, T. N., &
   Goldstein, M. L. 2019, ApJS, 242, 12
Cranmer, S. R., Gibson, S. E., & Riley, P. 2017, SSRv, 212, 1345
Cranmer, S. R., Kohl, J. L., Noci, G., et al. 1999, ApJ, 511, 481
Cranmer, S. R., Matthaeus, W. H., Breech, B. A., & Kasper, J. C. 2009, ApJ,
   702, 1604
Cranmer, S. R., & van Ballegooijen, A. A. 2010, ApJ, 720, 824
Cranmer, S. R., van Ballegooijen, A. A., & Woolsey, L. N. 2013, ApJ,
   767, 125
DeForest, C. E., Matthaeus, W. H., Viall, N. M., & Cranmer, S. R. 2016, ApJ,
Dobrzycka, D., Cranmer, S. R., Panasyuk, A. V., Strachan, L., & Kohl, J. L.
   1999, JGR, 104, 9791
Domingo, V., Fleck, B., & Poland, A. I. 1995, SoPh, 162, 1
Druckmüller, M., Habbal, S. R., & Morgan, H. 2014, ApJ, 785, 14
Elsässer, W. M. 1950, PhRv, 79, 183
Engelbrecht, N. E., & Strauss, R. D. T. 2018, ApJ, 856, 159
Faganello, M., & Califano, F. 2017, JPIPh, 83, 535830601
Feng, L., Inhester, B., & Gan, W. Q. 2013, ApJ, 774, 141
Fisk, L. A., Schwadron, N. A., & Zurbuchen, T. H. 1999, JGR, 104, 19765
Foullon, C., Verwichte, E., Nakariakov, V. M., Nykyri, K., & Farrugia, C. J.
   2011, ApJL, 729, L8
Foullon, C., Verwichte, E., Nykyri, K., Aschwanden, M. J., & Hannah, I. G.
  2013, ApJ, 767, 170
Fox, N. J., Velli, M., Bale, S. D., et al. 2016, SSRv, 204, 7
Frazin, R. A., Cranmer, S. R., & Kohl, J. L. 2003, ApJ, 597, 1145
Gardner, L. D., Smith, P. L., Kohl, J. L., et al. 2002, ISSIR, 2, 161
Giordano, S., & Mancuso, S. 2008, ApJ, 688, 656
Guhathakurta, M., Holzer, T. E., & MacQueen, R. M. 1996, ApJ, 458, 817
Hillier, A., & Polito, V. 2018, ApJL, 864, L10
Holzer, T. E., & Axford, W. I. 1970, ARA&A, 8, 31
Ismayilli, R. F., Dzhalilov, N. S., Shergelashvili, B. M., Poedts, S., &
   Pirguliyev, M. Sh 2018, PhPl, 25, 062903
Kohl, J. L., Esser, R., Gardner, L. D., et al. 1995, SoPh, 162, 313
Kohl, J. L., Noci, G., Antonucci, E., et al. 1998, ApJL, 501, L127
Kopp, R. A., & Holzer, T. E. 1976, SoPh, 49, 43
Kuridze, D., Zaqarashvili, T. V., Henriques, V., et al. 2016, ApJ, 830, 133
Leer, E., Holzer, T. E., & Fla, T. 1982, SSRv, 33, 161
Levine, R. H., Altschuler, M. D., Harvey, J. W., & Jackson, B. V. 1977, ApJ,
Li, X., Zhang, J., Yang, S., Hou, Y., & Erdélyi, R. 2018, NatSR, 8, 8136
Matsumoto, Y., & Hoshino, M. 2004, GeoRL, 31, L02807
```

```
McComas, D. J., Bame, S. J., Barraclough, B. L., et al. 1998, GeoRL, 25, 1
McKenzie, J. F., Banaszkiewicz, M., & Axford, W. I. 1995, A&A, 303,
  1.45
Miura, A., & Pritchett, P. L. 1982, JGR, 87, 7431
Möstl, U. V., Temmer, M., & Veronig, A. M. 2013, ApJL, 766, L12
Müller, D., St., Cyr, O. C., Zouganelis, I., et al. 2020, A&A, 642, A1
Noci, G., & Gavryuseva, E. 2007, ApJL, 658, L63
Nykyri, K., & Foullon, C. 2013, GeoRL, 40, 4154
Ofman, L., & Thompson, B. J. 2011, ApJL, 734, L11
Parhi, S., Suess, S. T., & Sulkanen, M. 1999, JGR, 104, 14781
Romoli, M., Antonucci, E., Andretta, V., et al. 2021, A&A, 656, A32
Ruffolo, D., Matthaeus, W. H., Chhiber, R., et al. 2020, ApJ, 902, 94
Ryutova, M., Berger, T., Frank, Z., Tarbell, T., & Title, A. 2010, SoPh, 267,
Schwadron, N. A., & McComas, D. J. 2021, ApJ, 909, 95
Schwenn, R., Inhester, B., Plunkett, S. P., et al. 1997, SoPh, 175, 667
Sheeley, N. R., Wang, Y.-M., Hawley, S. H., et al. 1997, ApJ, 484, 472
Smith, C. W., Isenberg, P. A., Matthaeus, W. H., & Richardson, J. D. 2006,
   ApJ, 638, 508
Strachan, L., Panasyuk, A. V., Kohl, J. L., & Lamy, P. 2012, ApJ, 745, 51
Suzuki, T. K., & Inutsuka, S.-I. 2005, ApJL, 632, L49
Suzuki, T. K., & Inutsuka, S.-I. 2006, JGRA, 111, A06101
Telloni, D., Andretta, V., Antonucci, E., et al. 2021, ApJL, 920, L14
Telloni, D., Antonucci, E., & Dodero, M. A. 2007a, A&A, 472, 299
Telloni, D., Antonucci, E., & Dodero, M. A. 2007b, A&A, 476, 1341
Telloni, D., Carbone, F., Bruno, R., et al. 2019a, ApJ, 887, 160
```

Telloni, D., Giordano, S., & Antonucci, E. 2019b, ApJL, 881, L36

```
Usmanov, A. V., Matthaeus, W. H., Goldstein, M. L., & Chhiber, R. 2018,
   ApJ, 865, 25
Velli, M., Lionello, R., Linker, J. A., & Mikić, Z. 2011, ApJ, 736, 32
Verdini, A., Velli, M., Matthaeus, W. H., Oughton, S., & Dmitruk, P. 2010,
  AnJL. 708, L116
Wenzel, K. P., Marsden, R. G., Page, D. E., & Smith, E. J. 1992, A&AS,
  92, 207
Withbroe, G. L. 1988, ApJ, 325, 442
Wang, Y.-M. 1994, ApJL, 437, L67
Wang, Y.-M., & Sheeley, N. R. 1990, ApJ, 355, 726
Wang, Y.-M., Sheeley, N. R., Socker, D. G., Howard, R. A., & Rich, N. B.
  2000, JGRA, 105, 25133
Yang, H., Xu, Z., Lim, E.-K., et al. 2018, ApJ, 857, 115
Yuan, D., Shen, Y., Liu, Y., et al. 2019, ApJL, 884, L51
Zank, G. P., Adhikari, L., Hunana, P., et al. 2017, ApJ, 835, 147
Zank, G. P., Adhikari, L., Hunana, P., et al. 2018a, ApJ, 854, 32
Zank, G. P., Adhikari, L., Zhao, L.-L., et al. 2018b, ApJ, 869, 23
Zank, G. P., Dosch, A., Hunana, P., et al. 2012, ApJ, 745, 35
Zank, G. P., le Roux, J. A., Webb, G. M., Dosch, A., & Khabarova, O. 2014,
    nJ. 797, 28
Zank, G. P., Matthaeus, W. H., & Smith, C. W. 1996, JGRA, 101, 17093
Zank, G. P., Nakanotani, M., Zhao, L. L., Adhikari, L., & Telloni, D. 2020,
  ApJ, 900, 115
Zank, G. P., Zhao, L.-L., Adhikari, L., et al. 2021, PhPl, 28, 080501
Zhao, L.-L., Zank, G. P., Adhikari, L., et al. 2020, ApJ, 898, 113
Zhao, L.-L., Zank, G. P., Chen, Y., et al. 2019, ApJ, 872, 4
Zhao, L.-L., Zank, G. P., Khabarova, O., et al. 2018, ApJL, 864, L34
```